Chemistry–A European Journal
Research Article
doi.org/10.1002/chem.202302039
Chemistry Europe
European Chemical Societies Publishing
www.chemeurj.org

Hot Paper

Synthesis, Characterisation, and Functionalisation of Charged Two-Dimensional MoS_2

Aleksandra M. Krajewska,[a] Aislan Esmeraldo Paiva,[a] Michael Morris,[a] and Aidan R. McDonald*[a]

The applications of exfoliated MoS_2 are limited by its inert surface and poor interface. We have activated the surface of exfoliated 2H-MoS_2 by reacting it with $NaBH_4$, forming an n-doped material as demonstrated by a negative zeta-potential value $\zeta = -25$ mV and a 20 nm (0.05 eV) red-shift in its photo-luminescence spectrum. The novel material's spectral properties were consistent with pristine 2H-MoS_2 (as determined by HR-TEM, XPS, pXRD, DRIFT, TGA, and Raman spectroscopy). Importantly, it was readily dispersed in H_2O unlike 2H-MoS_2. Its dispersibility properties were explored for a variety of solvents and could be directly correlated with the relative permittivity of the respective solvents. The charged 2H-MoS_2 reacted readily with an organo-iodide to deliver functionalized 2H-MoS_2. Our approach delivers aqueous dispersions of semiconducting 2H-MoS_2, without additives or chemical functionalities, and allows for controlled and facile functionalization of 2H-MoS_2 opening multiple new avenues of semi-conducting MoS_2 application.

Introduction

MoS_2 has attracted significant attention for applications in energy,[1] electronics,[2,3] catalysis,[4,5] and biomaterials sectors,[6,7] due to its versatile electronic properties as well as its abundance in the crust. MoS_2, as with other transition metal dichalcogenides (TMDs), displays a graphene-like layered structure which can be exfoliated to yield two-dimensional (2D) flakes that display desirable properties, including conversion to a direct bandgap and a significant increase in the availability of catalytically active sites.[8–10] In its natural state, MoS_2 exists as the 2H-polymorph, with trigonal prismatic geometry at Mo, which is a semi-conductor. 2D semiconducting 2H-MoS_2 can be prepared through liquid-phase exfoliation, amongst other methods.[11–13] A reduction followed by re-oxidation of bulk 2H-MoS_2 yields the 1T-phase which displays octahedral geometry at Mo, and due to a change in the orbital splitting, is metallic. Through chemical reduction it is possible to access monolayers of 1T-MoS_2. This process is called chemical exfoliation, where the reaction of reduced MoS_2^{x-} with H_2O facilitates gas evolution-driven exfoliation, yielding 1T-MoS_2.[14] Recently some strategies yielded a distorted octahedral geometry at Mo, known as 1T′-MoS_2, which has semi-metallic properties.[15] The 2D forms of MoS_2 have varied applications: 2H-MoS_2 in printed electronics,[16] optoelectronics,[17] and gas sensors;[18] and 1T-MoS_2 in batteries,[19] supercapacitors,[20] energy conversion systems,[21] and as a hydrogen evolution catalyst.[22]

Each of the polymorphs has its limitations: 1T-MoS_2 suffers from instability caused by its metastable nature and high level of defects, which limits its implementation in scaled-up and long-lived systems. 2H-MoS_2, on the other hand, due to the inertness of its surface is challenging to implement into more complex devices, creating a poor interface with the other components. 2H-MoS_2 is poorly dispersible in common solvents, including H_2O, which inhibits the development of aqueous applications in drug delivery, cancer treatment, photo-thermal therapy, or imaging.[23,24] Some strategies were implemented to exfoliate bulk MoS_2 in H_2O, however, they suffer from low yields, short stability, and a lack of control over the lateral size and thickness of the obtained flakes.[25–27] Furthermore, for the catalysed hydrogen evolution reaction (HER), 2H-MoS_2 has fallen short in comparison to 1T-MoS_2 with its excellent conductivity and catalytically active basal plane.[28–31]

One approach to enhance the applicability of 2H-MoS_2 is through functionalization. For a long time this was impossible for 2H-MoS_2 due to its chemical inertness and a lack of defects at the surface, which allowed only for either physisorption or formation of dative interactions.[32,33] In the meantime, many adaptable strategies were developed for the 1T-polymorph, where the mechanism was driven by the reaction between the negatively charged surface and electrophiles.[34,35] Recently some methods of covalent functionalization of 2H-MoS_2 were proposed by reactions with maleimides and aryl diazonium salts.[36,37] These strategies, however, offer either limited scope of (rather complex) substrates or are not suitable for liquid-processed samples, restricting the scale and applicability of the reaction. Herein, we demonstrate methods for the activation of the surface of 2H-MoS_2 to tackle some of the limitations resulting from the inertness of the material. The activated 2H-

[a] A. M. Krajewska, A. E. Paiva, Prof. M. Morris, Prof. A. R. McDonald
CRANN/AMBER Nanoscience Institute and School of Chemistry
Trinity College Dublin
The University of Dublin
College Green, Dublin 2 (Ireland)
E-mail: aidan.mcdonald@tcd.ie
Homepage: https://chemistry.tcd.ie/staff/people/mcdonald

Supporting information for this article is available on the WWW under https://doi.org/10.1002/chem.202302039

MoS_2 demonstrates many of the advantages associated with 1T-MoS_2 while maintaining the semi-conducting phase of the 2D nanomaterial.

Results and Discussion

Preparation of novel exfoliated MoS_2

Pristine 2H-MoS_2 was prepared through liquid-phase exfoliation of bulk MoS_2 in propan-2-ol (IPA), according to a previously reported method.[33,38] Bulk MoS_2 was tip-sonicated for 5 h, yielding a stable dispersion of 2H-MoS_2 with flakes demonstrating a mean lateral size of $L = 260$ nm.[33] The electronic absorption spectrum of dispersed 2H-MoS_2 displayed bands characteristic of liquid-exfoliated few-layer 2H-MoS_2: $\lambda_A =$ 674 nm, $\lambda_B = 614$ nm, $\lambda_C = 457$ nm and $\lambda_D = 406$ nm (Figure S1).[38] The mean number of layers in the flakes was determined to be ~10, as estimated from the position of λ_A,[39] aligning with the previously reported AFM analysis (9–10 layers).[33] The average concentration of the dispersion was determined to be 0.40–0.45 g L^{-1} using the absorptivity at $\lambda =$ 345 nm.[38] The pristine 2H-MoS_2 was further characterised by transmission electron microscopy (TEM, Figure S2). The material displayed a flake morphology typical for liquid-phase exfoliated samples of 2H-MoS_2.[11,39] High resolution TEM (HR-TEM) displayed clearly visible lattice fringes, corresponding to the d-spacing of the [100] crystal plane of 2H-MoS_2 (Figure S3).[40] Moreover, the fast Fourier transform (FFT) image presented a diffraction pattern characteristic of the 2H-polymorph of MoS_2.[41]

In order to explore routes to chemically activate and/or modify 2H-MoS_2, we reacted the acquired 2H-MoS_2 dispersion with $NaBH_4$ (Scheme 1). We envisaged the reductant $NaBH_4$ would provide access to novel avenues of chemical modification of MoS_2. A dispersion of 2H-MoS_2 in IPA (0.40 g L^{-1}) was mixed with solid $NaBH_4$ at 25 °C for 24 h. This led to the flocculation of the nanomaterial in IPA, as determined through visual analysis, indicating a change in its surface properties (Figure 1). The IPA was removed by centrifugation allowing for the isolation of a black solid that was redispersed in deionised H_2O (flocculation/aggregates were not observed in the obtained aqueous dispersion). For comparison, pristine 2H-MoS_2 did not form a stable dispersion in H_2O and flocculated readily upon introduction to the solvent. These observations indicated that

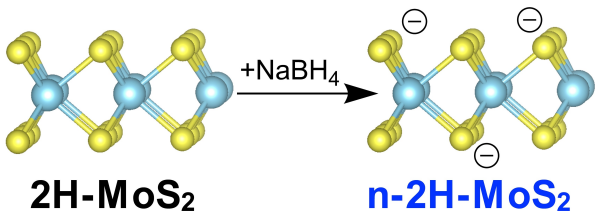

Scheme 1. The reaction of liquid exfoliated 2H-MoS_2 with $NaBH_4$ to yield n-2H-MoS_2.

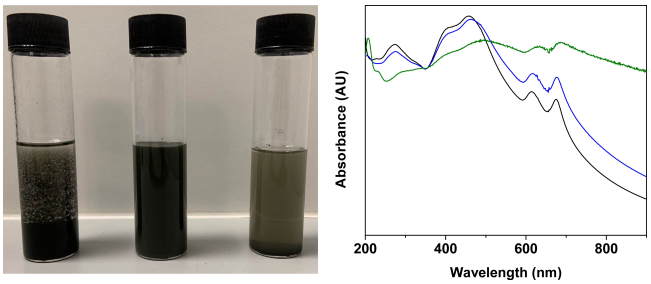

Figure 1. Left: visual assessment of dispersibility of n-2H-MoS_2 after the reaction of pristine 2H-MoS_2 with $NaBH_4$ in IPA (left), redispersion of n-2H-MoS_2 in H_2O (middle), and an attempt to disperse pristine 2H-MoS_2 in H_2O (right); Right: electronic absorption spectra of n-2H-MoS_2 in H_2O (blue), pristine 2H-MoS_2 in IPA (black), and pristine 2H-MoS_2 redispersed in H_2O (green). All the spectra were normalised to the local minimum at $\lambda = 345$ nm for ease of comparison.

$NaBH_4$ had reacted with pristine 2H-MoS_2 yielding a product that was readily dispersed in H_2O.

The electronic absorption spectrum of the re-dispersed material from the reaction of 2H-MoS_2 with $NaBH_4$ in H_2O showed that the product of the reaction displayed almost identical absorption features to pristine 2H-MoS_2 in IPA (Figure 1). The four spectral features commonly associated with liquid-exfoliated 2H-MoS_2 were present at $\lambda = 675$ nm, 615 nm, 460 nm and 410 nm, corresponding to λ_A, λ_B, λ_C, and λ_D, respectively.[38] Furthermore, the absorption spectrum confirmed our visual observation that the new material was very well dispersed in H_2O. A minimal baseline shift and a 1 nm red-shift of λ_A and λ_B were noted. In contrast, the electronic absorption spectrum of pristine 2H-MoS_2 in H_2O showed large spectral deviations compared to the starting dispersion of pristine 2H-MoS_2 in IPA (Figure 1). A large baseline shift and red-shift (15 nm) for λ_A and λ_B indicated the agglomeration of the nanomaterial. In summary, the reaction between 2H-MoS_2 and $NaBH_4$ resulted in the formation of a novel 2H-MoS_2 that was well-dispersed in H_2O, apparently as a result of a change in the surface properties of the new nanomaterial. We have defined the novel material as n-2H-MoS_2 for reasons that are defined below.

The electronic absorption spectrum of n-2H-MoS_2 did not exhibit any new features. No new transition was observed in the high-energy (ultra-violet) region. This excludes the possibility of the phase transformation from the 2H to the 1T polymorph of MoS_2. 1T-MoS_2 exhibits transitions at $\lambda = 260$ nm and $\lambda = 300$ nm, that tail into the visible, but with no other transitions observed in the visible/near-infra-red (NIR).[42] A phase transition to 1T-MoS_2 might have been expected: exfoliated 1T-MoS_2 is commonly prepared from the reduction of bulk MoS_2 with ^{n}BuLi,[14] or by electrochemical means,[43] or through reduction by Na/K alloy.[44] Despite using a reducing agent in this experiment (on pre-exfoliated 2H-MoS_2), no phase transition was observed. We conclude that while a chemical change has occurred on the surface of the liquid-exfoliated 2H-MoS_2, it has not triggered a phase transition to the 1T-polymorph.

A zeta-potential measurement was carried out to understand the surface properties of n-2H-MoS_2. It displayed a sharp peak ~−25 mV (Figure 2), indicating the localization of negative charge on the surface of the new material. This charge localization might explain n-2H-MoS_2's newfound hydrophilicity – the presence of the charge may increase the contribution of the electrostatic interaction in the stabilization of the new dispersion in H_2O. The dispersion of pristine 2H-MoS_2 in IPA exhibited a very broad zeta-potential distribution, stretching from −150 mV to +100 mV. Such a wide charge range indicated that the dispersion of 2H-MoS_2 was not stabilised by electrostatic forces, suggesting a relatively inert and uncharged surface, as would be expected for pristine 2H-MoS_2. Interestingly, zeta-potential measurements for dispersions of 1T-MoS_2 in H_2O demonstrated a similar sharp peak with a value of ~−40 eV.[35,45] In those reports, the negative zeta-potential was linked to the localization of negative charge at the surface of 1T-MoS_2. A good dispersibility in H_2O and the negative zeta-potential in n-2H-MoS_2 have indicated that there is some negative charge on the surface of the product of the reaction of pristine 2H-MoS_2 with $NaBH_4$, leading us to define the new material as a negatively-charged 2H-MoS_2 (n-2H-MoS_2).

The laser-induced photoluminescence properties of n-2H-MoS_2 were measured to gain some information about the electronic structure of the bandgap in the novel material (Figure 2). Photoluminescence emissions were observed in the 610–730 nm range (1.7–2.0 eV), confirming the preservation of semiconducting properties in n-2H-MoS_2. Two emissions (normally characteristic of 2H-MoS_2) were identified: $\lambda = 705$, 630 nm, both corresponding to photoluminescence from the direct bandgap.[8] Interestingly, the photoluminescence spectrum of pristine 2H-MoS_2 displayed a slightly lower energy emission band, centred at $\lambda = 685$ nm. This shift by 20 nm (0.05 eV) is direct evidence of n-doping in n-2H-MoS_2.[46] The same shift has been previously correlated with the increased population of negatively charged trions over neutral excitons in the emission spectrum of chemically doped 2H-MoS_2. This indicates the presence of a surplus of electrons in n-2H-MoS_2, which could localise at the surface of the material in the form of the negative charge density, as detected by the zeta-potential measurement.

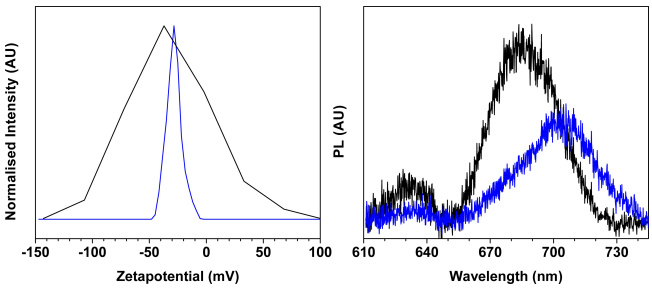

Figure 2. The zeta-potential distribution (left) and photoluminescence (right) of n-2H-MoS_2 (blue) and pristine 2H-MoS_2 (black).

Optimization of the reaction

The experimental conditions for the reaction between pristine 2H-MoS_2 and $NaBH_4$ were optimised (Figures S4–S10). To follow the optimisation process accurately using electronic absorption spectroscopy, the molar extinction coefficient for n-2H-MoS_2 in H_2O was determined and was found to equal $\varepsilon = 35.7$ (2.8) $L\,g^{-1}\,cm^{-1}$ as measured at the local minimum $\lambda = 345$ nm (Figure S4). To probe the effect of $NaBH_4$ concentration, two concentrations of $NaBH_4$ reacting with a 2H-MoS_2 dispersion were examined: 7.5 mM and 75 mM (Figure S5). The lower concentration of $NaBH_4$ yielded a less stable dispersion that partially agglomerated after 1 week of storage at 5 °C, whereas the higher concentration did not, indicating a better stability of n-2H-MoS_2. The optimal reaction time was probed by mixing the reactants for 3, 5, 16 and 24 h. An increase in the concentration of the formed n-2H-MoS_2 as well as improved dispersibility was demonstrated with the increased mixing times (Figure S6). After 4 days of storage at 5 °C, no change in the concentration or the dispersibility of the samples was detected, indicating that the time of the reaction did not affect the long-term stability of the samples. The n-2H-MoS_2 products obtained under the optimised conditions displayed very good long-term stability (Figures S7 and S8).

Two catalyst additives (for $NaBH_4$ activation) and a change in reaction temperature were then examined: methanol, acetic acid, or increasing the temperature of the reaction to 60 °C. All yielded dispersions with *worse* dispersibility of n-2H-MoS_2 compared to the control dispersion (Figure S9). This indicated that the addition of reagents promoting the activation of $NaBH_4$ negatively impacted the reaction between $NaBH_4$ and 2H-MoS_2. Lastly, we examined whether our method would work on 2H-MoS_2 sourced from an alternative liquid exfoliation solvent. Hence, we exfoliated 2H-MoS_2 in *N*-methyl-2-pyrolidone (NMP) through liquid-phase exfoliation and reacted the obtained 2H-MoS_2 dispersion with $NaBH_4$. The obtained n-2H-MoS_2 was again very well dispersed in H_2O, as demonstrated by the electronic absorption spectrum and the formation of a sharp peak during the zeta-potential measurement at ~−30 mV (Figure S10), indicating the successful localisation of negative charge on the surface. Overall, we established that both an increased concentration of $NaBH_4$ and a longer time of reaction were beneficial for the stability and concentration of n-2H-MoS_2 in H_2O, however, the use of $NaBH_4$ activators was detrimental, and finally, our method is applicable to dispersions from multiple solvent sources.

We postulate that the mechanism of the reaction that takes place between $NaBH_4$ and exfoliated 2H-MoS_2, involves nucleophilic hydride attack (from $^{-}BH_4$) at an S-vacancy to yield a reduced anionic form of 2H-MoS_2, tentatively defined as r-2H-MoS_2 (Na[H-MoS_2]). This presumably results in the formation of a Mo–H adduct at the S-vacancy. The addition of H_2O to the reaction mixture to quench excess $NaBH_4$, presumably converts the Mo–H adduct to H_2 (accounting for the observation of gas-evolution), n-2H-MoS_2, and NaOH. The formed n-2H-MoS_2 presumably maintains some of the negative charge associated with the reduced form, mirroring the conversion of $Li_x[MoS_2]^x$ to

1T-MoS_2 during the chemical exfoliation of MoS_2, where the negative charge in 1T-MoS_2 is a residual associated with the negatively charged $[MoS_2]^{x-}$.[47]

Characterization of n-2H-MoS_2

TEM images of n-2H-MoS_2 were collected to examine the morphology and crystallinity of the nanomaterial after the reaction with $NaBH_4$ (Figure 3). The TEM images revealed a minor change in the flake morphology, as the sheets appeared more folded and crumpled in comparison to pristine 2H-MoS_2. Similar images have previously been presented for chemically treated flakes of MoS_2,[34,40] or flakes liquid-exfoliated in NMP.[48,49] An analysis of high-resolution (HR)-TEM images revealed that the crystalline structure was preserved in n-2H-MoS_2, as indicated by the visible lattice fringes displaying 0.28 nm d-spacing, characteristic of the [100] lattice plane of 2H-MoS_2 (Figure 3). The same d-spacing was calculated from the FFT image. In addition, no visible deterioration of the n-2H-MoS_2 surface was observed. Moreover, the images displayed the formation of some moiré patterns caused by folding and stacking of the flakes on top of each other in a random orientation (Figure S11). This has also been visualised in the FFT images where the main diffraction spots were accompanied by smaller ones, indicating twisting of the planes between the stacked layers.

Due to the significant folding and stacking displayed in the TEM images, it was not possible to determine the thickness and lateral size of the individual flakes of n-2H-MoS_2 through microscopy. However, dynamic light scattering (DLS) measurements allowed us to estimate the particle size in the dispersion. For pristine 2H-MoS_2 the mean lateral size and thickness were established as 260 nm and 9.5 layers respectively by AFM.[33] DLS results displayed a minimal difference in the size distribution in n-2H-MoS_2 compared to pristine 2H-MoS_2 (Figure S12, 200 nm versus 180 nm, respectively). Importantly, both samples displayed monomodal size distribution with no agglomeration visible in the solution. It is an important comparison indicating that the stacking observed in TEM occurs only after drop-casting of the sample – flakes appear well-dispersed in solution. Moreover, no significant fragmentation occurred after the reaction with $NaBH_4$, as no increase in the population of small particles was observed.

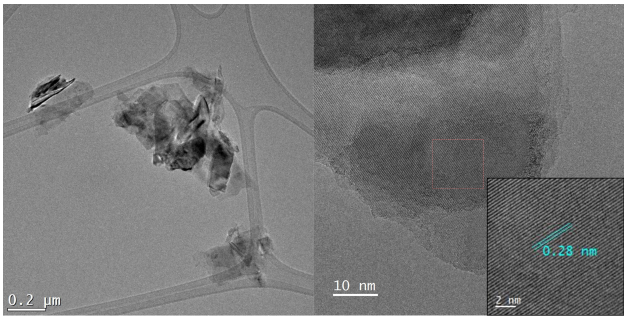

Figure 3. TEM image of n-2H-MoS_2 (left) and HR-TEM image of n-2H-MoS_2 depicting an edge site (right). Inset is the magnified image of the area inside the square.

The X-ray photoelectron spectroscopy (XPS) survey spectra of both n-2H-MoS_2 and 2H-MoS_2 (Figure S13) showed the presence of Mo, S, C and O atoms. n-2H-MoS_2 did not contain any new elements compared to pristine 2H-MoS_2. Notably, there were no signals from either Na or B, demonstrating that any $NaBH_4$ decomposition products as well as any unreacted material were successfully removed. There was no significant increase in the C and O components detected at the surface of n-2H-MoS_2 either, indicating that the surface was not functionalised with hydrocarbons or hydroxy groups, nor was it contaminated with carbonaceous materials during the reaction. The survey spectrum also revealed the Mo:S ratio to be 1:1.9 for both n-2H-MoS_2 and pristine 2H-MoS_2, suggesting that no new S-vacancies and/or defects were introduced during the reaction. Overall, the XPS survey spectrum indicated there was no difference in the elemental composition of n-2H-MoS_2, compared to pristine 2H-MoS_2.

The Mo 3d and S 2p core level spectra of n-2H-MoS_2 did not reveal any signs of chemical change (Figure S14) – there were no new Mo or S components present, moreover, there was no change in the width of the fitted components proving that no new features were hiding under the simulated fit. This shows that the Mo and S coordination sphere stayed unchanged after the reaction with $NaBH_4$, and there was no change in the oxidation state or bonding in the final product. It also suggests that no transition to the 1T-MoS_2 polymorph had occurred. Despite evidence of a negative charge in n-2H-MoS_2 as demonstrated by the zeta-potential measurement, emission spectroscopy, and dispersibility studies (below), no shift in the energy of the Mo or S core level spectra was observed. It is important to note that the zeta-potential magnitude in n-2H-MoS_2 was noticeably lower than the zeta-potential data previously observed for 1T-MoS_2. This would suggest that the amount of the charge localised at the surface of n-2H-MoS_2 is less than in 1T-MoS_2, where XPS shows an apparent ~0.8 eV shift to lower energy for both Mo and S core level spectra.[42] In n-2H-MoS_2 the delocalised charge is not significant enough to noticeably alter the binding energy of the core orbitals.

Powder X-ray diffraction (pXRD) was carried out to investigate any possible changes in the crystalline phase in n-2H-MoS_2 (Figure S15). The pXRD spectrum of n-2H-MoS_2 overlapped perfectly with the spectrum of 2H-MoS_2. There were no new peaks present – excluding the possibility of ion intercalation, conversion to the 1T-phase, or other phase changes to the material. No change in the peak position or their width was observed, indicating that there was no difference in the interlayer distances (frequently observed after the covalent functionalization of various nanomaterials).[50,51] The lack of broadening proved that there was no loss in the crystallinity of the material – it has not been functionalised, no new defects were introduced, nor was there a significant decrease in the number of layers.[40]

Thermogravimetric analysis (TGA) and diffuse reflectance infrared Fourier transform spectroscopy (DRIFT) also did not provide any evidence for the presence of any new moieties at

the surface of the material after the reaction (Figures S16 and S17). The TGA decomposition profile did not show any additional mass loss in n-2H-MoS_2 in comparison to 2H-MoS_2. Similarly, DRIFT did not present any new vibrations from any new possible functionalities. At the same time, all the vibrations visible in the pristine 2H-MoS_2 sample were preserved in n-2H-MoS_2. Most importantly the Mo–S vibration at $\tilde{\nu} = 384\ cm^{-1}$ (corresponding to the in-plane stretching mode) was observed in n-2H-MoS_2,[52] which emphasises that the crystallinity of the lattice was maintained.

Raman spectroscopy was carried out on n-2H-MoS_2 with the $\lambda = 633$ nm laser line (Figure S18). All of the characteristic 2H-phase vibrations (E^1_{2g}, A_{1g} and 2LA(M)) were observed in the n-2H-MoS_2 sample. The normalised spectrum displayed a modest decrease in the intensities of E^1_{2g} and 2LA(M) peaks in comparison to pristine 2H-MoS_2. It has been proposed that such increased interactions of the photons with the A_{1g} phonon might be a result of a change in the band structure of the material.[53] This is a possible outcome of the negative doping in n-2H-MoS_2. Previous reports showed a decrease in the 2LA(M)/A_{1g} intensity ratio was correlated with the functionalization of MoS_2.[34,54,55] Those reports, however, depict a significant consumption of the 2LA(M) vibrational mode, with no effect on the E^1_{2g} peak intensity. We conclude that the decrease in the 2LA(M) peak intensity is not indicative of the surface functionalization but is a result of a negative charge influencing the band structure of n-2H-MoS_2. Finally, the characteristic phonons for the 1T-phase ($\tilde{\nu}_1 = 156\ cm^{-1}$, $\tilde{\nu}_2 = 226\ cm^{-1}$, $\tilde{\nu}_3 = 333\ cm^{-1}$) were absent.[56] In total, Raman spectroscopy demonstrated that n-2H-MoS_2 has preserved the semiconducting phase, although a modest impact on the bandgap is evident.

In summary, the collected characterization showed that negative charge density has been introduced to the surface of the semiconducting phase of 2H-MoS_2. The density of charge localised at the surface does not match that previously reported for 1T-MoS_2, however, it is sufficient to mimic the 1T-MoS_2 surface properties. This change in the surface chemistry has been achieved without a phase change, and moreover, without decomposition of the nanomaterial, introduction of significant defects, *or* chemical functionalization of the surface. n-2H-MoS_2 thus represents a promising novel form of 2D TMDs.

Probing dispersibility of exfoliated MoS_2 in common solvents

The differences in dispersibility of pristine 2H-MoS_2 and n-2H-MoS_2 in H_2O motivated us to examine the dispersibility of both materials, together with chemically exfoliated 1T-MoS_2 in other solvents. 1T-MoS_2 was synthesised through the reaction of bulk MoS_2 with ^{n}BuLi adapting a literature procedure.[14] The electronic absorption spectra of the nanomaterials in the appropriate solvents were used to compare their dispersibility. The baseline shift above '0' absorption units is related to the light scattering effect of the nanoparticles, and hence, can provide insight into the dispersibility of a nanomaterial in a given solvent. n-2H-MoS_2, 2H-MoS_2, and 1T-MoS_2 were dispersed in solvents displaying varying physical attributes: H_2O, IPA, dimethyl sulfoxide (DMSO), CH_3CN, acetone, toluene, NMP and diethyl ether (Et_2O). All spectra were normalised at $\lambda = 345$ nm and the absorbance at $\lambda = 800$ nm (the gauge of the baseline shift) of each sample was measured and compared, to assess the relative dispersibilities.

n-2H-MoS_2 displayed a varying baseline shift depending on the dispersing solvent, indicating varying degrees of dispersibility (Figure 4). The lowest baseline shift was observed for NMP, closely followed by H_2O and DMSO. A slightly higher baseline absorbance was then observed for IPA, CH_3CN and acetone. Lastly, a significantly higher baseline shift was noted for Et_2O and toluene, with toluene displaying complete bleaching of the characteristic $\lambda_{A\text{-}D}$ transitions. Thus, apolar solvents were incompatible with n-2H-MoS_2, while polar solvents proved to be much more appropriate.

The dispersibility of pristine 2H-MoS_2 in the same solvents was also examined (Figure 4). The lowest baseline shift was again observed in NMP, as well as CH_3CN, IPA, and acetone. However, in contrast to n-2H-MoS_2, a noticeably higher baseline absorbance was observed both for DMSO and H_2O, two of the most polar solvents from the examined range. Lastly, the highest baseline was noted for Et_2O and toluene. Overall, a clear change in the solvent affinity after activation of the surface of 2H-MoS_2 was noted, with n-2H-MoS_2 displaying a much better dispersibility in polar solvents than pristine 2H-MoS_2. The dispersibility of 1T-MoS_2 was also examined (Figure 4). 1T-MoS_2 displayed the lowest baseline shift in NMP, H_2O, and DMSO, and the highest baseline absorbance was observed for Et_2O and toluene. In general, 1T-MoS_2 demonstrated similar dispersibility to n-2H-MoS_2, suggesting that the negative charge in both materials facilitates their dispersion in more polar solvents.

To examine the change in the surface chemistry in more detail, the relative dispersibility (absorbance at $\lambda = 800$ nm for each solvent, normalised against the absorbance in H_2O) was plotted as a function of various parameters that are known to affect the dispersibility: dipole moment, polarizability, surface tension, Hansen solubility parameters, and relative permittivity (dielectric constant). In most cases, no clear trend was observed (Figures S19–S24), apart from the relative permittivity, where a reasonably predictable relationship was noted. To quantitatively represent this trend the data was fitted with a simple exponential fit (Figure S25). The exponential fit was much better for n-2H-MoS_2 and 1T-MoS_2 than pristine 2H-MoS_2.

In the context of DLVO theory, relative permittivity is linked to the diffuse double layer forces (electrostatic interactions), which are responsible for the stabilisation of the colloidal dispersions. It can be related through an exponential function to the surface potential. Equation (1) describes the change in electric potential distribution with the increasing distance from the charged surface in the diffuse double layer:[57]

$$\psi = \psi_0 \exp[-\kappa x] \quad (1)$$

where Ψ_0 is the potential of the surface, x is the distance from the surface, Ψ is the potential at the distance x, and κ is described by Equation (2):

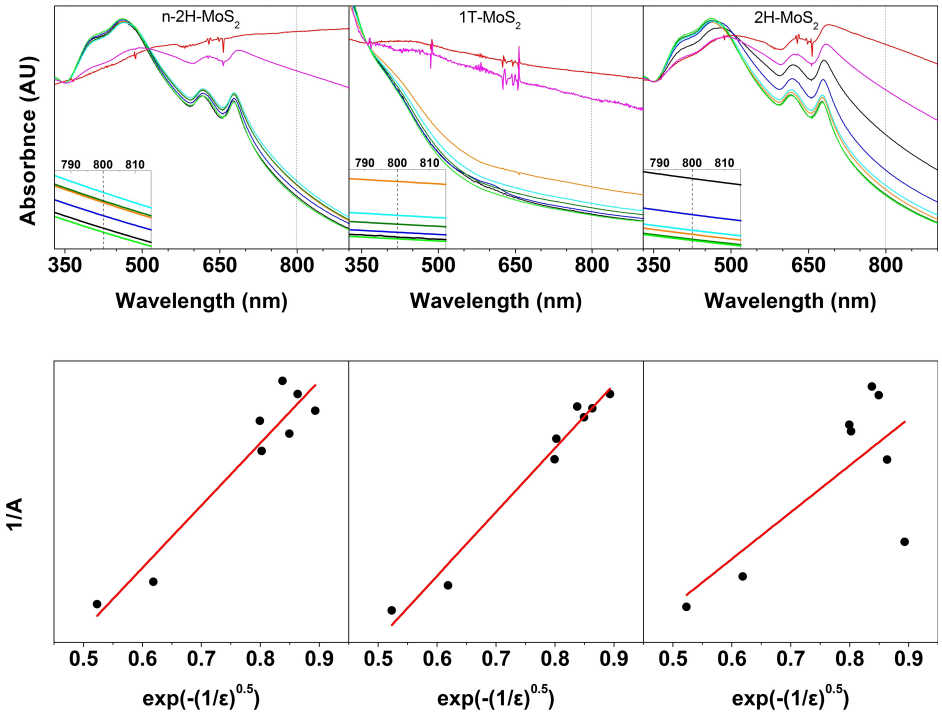

Figure 4. Top: Electronic absorption spectra of the nanomaterials after redispersion in a range of solvents. Colour Code: H_2O (black), DMSO (blue), NMP (light green), CH_3CN (green), acetone (cyan), IPA (orange), Et_2O (magenta) and toluene (red). All spectra were normalised to the local minimum, $\lambda = 345$ nm. Inset are the magnified regions around 800 nm displaying fine differences in the baseline shift. Bottom: the linear relationship of stability of the dispersion of the nanomaterial with the exponent of relative permittivity of solvents for n-2H-MoS_2 (left), 1T-MoS_2 (middle) and 2H-MoS_2 (right). The adjusted R^2 values were 0.91, 0.97, and 0.44, respectively.

$$\kappa = \left(\frac{2e^2 n_0 z^2}{\varepsilon kT}\right)^{\frac{1}{2}} \quad (2)$$

where ze is the charge of the examined species, n_0 is the concentration of the charged species, k is the Boltzmann constant, T is the temperature (all of those have the same value for all samples in a given series), and ε is the relative permittivity of the solvent. This allows us to relate the surface potential to the relative permittivity through the proportion (Equation (3)):

$$\psi \sim exp\left(-\sqrt{\frac{1}{\varepsilon}}\right) \quad (3)$$

If we assume the baseline absorptivity is inversely proportional to the surface potential (Equation (4)), then Equation (5) should yield a linear plot of absorptivity against relative permittivity:

$$stability \sim \psi \sim \frac{1}{A} \quad (4)$$

$$\frac{1}{A} \sim exp\left(-\sqrt{\frac{1}{\varepsilon}}\right) \quad (5)$$

Hence, the above relationship was plotted for n-2H-MoS_2, 2H-MoS_2, and 1T-MoS_2 redispersed in various solvents (Figure 4). A linear relationship was observed for n-2H-MoS_2 and 1T-MoS_2. Pristine 2H-MoS_2 displayed a poor correlation, presumably due to a lack of charge on the surface. In the context of DLVO theory, the good correlation of n-2H-MoS_2 and 1T-MoS_2 with the relative permittivity demonstrates clear dependence and dominance of the double layer over van der Waals forces which grants enhanced stability of these colloidal dispersions. Notably the electrical double layer forces are known to increase with the surface charge density, which also explains a marginally better correlation with 1T-MoS_2 over n-2H-MoS_2 and complete lack of correlation in the case of 2H-MoS_2. This complements our zeta-potential measurements where the magnitude of charge detected at the surface of n-2H-MoS_2 was lower than the charge detected at the surface of 1T-MoS_2. This analysis provides further evidence for successful charge localisation at the surface of n-2H-MoS_2.

Applications of n-2H-MoS_2

The application of n-2H-MoS_2 as a catalyst for the HER was explored (alongside 2H-MoS_2 and 1T-MoS_2). A three-electrode set-up was employed with glassy carbon as a working electrode, Pt wire as a counter electrode, and Ag/Ag^+ as a reference electrode (see experimental methods for details). The catalysts were drop-cast onto the glassy carbon (Figure S26). Linear sweep voltammetry (LSV) was carried out and the obtained polarization curves were used to determine the onset potential, the overpotential and the Tafel slope (Table S1,

Figure S27). Overall, little difference was observed in the performance of n-2H-MoS_2 and 2H-MoS_2. 1T-MoS_2 displayed a much lower onset potential than n-2H-MoS_2 and 2H-MoS_2, which is consistent with previous reports.[28,29,58] The enhanced negative charge density in n-2H-MoS_2 appears to have had little impact on HER effectiveness. These results indicate that neither the kinetics nor the mechanism of the HER reaction were affected by the introduction of negative charge. It also indicated that the reaction with $NaBH_4$ did not activate the basal plane of the 2H-MoS_2. On the other hand, n-doping in n-2H-MoS_2 did not influence the catalytic performance in a negative way either. Previous reports showed an improvement in the performance of 1T-MoS_2 after quenching of the negative charge.[29] This would suggest that charge may not play an important role in HER catalysed by 2H-MoS_2 and that morphology and concentration of defect sites may be more important in enhancing the catalytic activity.

Lastly, we found that n-2H-MoS_2 was an excellent candidate for the functionalization of 2H-MoS_2. n-2H-MoS_2 was reacted with 3-(iodomethyl)pyridine yielding pyridyl-functionalized 2H-MoS_2 (py-2H-MoS_2). For py-2H-MoS_2, the TGA curve displayed a clear additional mass loss of 1.5–2 wt% compared to n-2H-MoS_2 (Figure S28). The mass loss was detected above 250 °C, indicating a covalent tethering of the functionality. The degree of functionalization was lower than achieved by Chhowalla and co-workers (~5 wt%), which we ascribe to the lower concentration of charge on the surface in n-2H-MoS_2. The DRIFT spectrum of py-2H-MoS_2 displayed new features at $\nu =$ 1637 cm^{-1} and 1506 cm^{-1} (corresponding to C=N and C=C vibrations in the pyridine ring, Figure S29). The reaction with organo-iodides mirrors the method developed by Chhowalla for the functionalization of 1T-MoS_2, where negative charge in 1T-MoS_2 was reacted as a nucleophile.[35] This approach was previously inaccessible for 2H-MoS_2. Our results are an important breakthrough demonstrating the functionalization of pristine 2H-MoS_2 and introduces a facile method for the further engineering of 2H-MoS_2.

Conclusions

We describe the preparation of a novel 2D semiconducting 2H-MoS_2 that was formed upon the reaction of liquid-exfoliated 2H-MoS_2 with $NaBH_4$. The derivatized material demonstrated excellent dispersibility in H_2O, which is uncommon for 2H-MoS_2. The enhanced dispersibility and doping were ascribed to the introduction of negative charge on the surface of 2H-MoS_2. Furthermore, photoluminescence spectroscopy suggested n-doping of the material. Extensive characterization with electronic absorption spectroscopy, TEM, XPS, pXRD, TGA, DRIFT and Raman spectroscopy revealed no signs of defects, or deterioration in the novel material, defined as n-2H-MoS_2. The dispersibility of n-2H-MoS_2 in common solvents beyond H_2O revealed better stability in solvents with higher dielectric constants, with a direct correlation between the solvent dielectric constant and the measured dispersibility. The introduction of charge also allowed for facile covalent functionalization of semiconducting 2H-MoS_2 using methods that, until now, were only suitable for metallic 1T-MoS_2. The facile n-doping and aqueous dispersibility of the novel 2D semiconducting MoS_2 make it a promising candidate for application in aqueous (biological) applications as well as printed electronics, transistors, or light emitting diodes.

Experimental Section

Physical methods: Electronic absorption spectra were collected in 1 cm quartz cuvettes using an Agilent 8453 Diode Array Spectrophotometer. High resolution transmission electron microscopy (HR-TEM) images were obtained with FEI Titan microscope at 300 kV acceleration voltage (G2 80-300FEG S/TEM). Zeta-potential and Dynamic light scattering (DLS) measurements were performed with Malvern Zetasizer Nano ZS at 25 °C. For photoluminescence measurements, a WITec alpha300 R Raman microscope with 532 nm laser at 30 mW laser power was used. X-ray photoelectron spectroscopy (XPS) was performed under ultra-high vacuum ($< 5\times10^{-10}$ mbar) on a VG Scientific ESCAlab Mk II system with an Al K_α X-ray source (1486.6 eV, CTX400, PSP Vacuum Technology). Survey spectra were collected at 100 eV sweep energy and core level spectra were collected at 50 eV. All spectra were calibrated to the C 1s core level orbital at 284.8 eV. Spectra were fitted with Shirley background and Gaussian-Lorentzian function. Powder X-ray diffraction (pXRD) spectra were collected on a Bruker D2 Phaser with Cu Kα radiation ($\lambda = 1.54178$ Å) at 30 kV, 10 mA with the LynxEye detector, in the range 5–70° in 2θ, using a 0.01° increment at 0.5 s per step. Thermogravimetric analysis (TGA) was performed on the Perkin Elmer Pyris 1 TGA Thermogravimetric Analyser. All measurements were carried out under nitrogen gas at a heating rate of 20 °C/min in a 100–800 °C temperature range. Directly before the data collection the temperature was set for 5 min to 100 °C to facilitate the evaporation of any residual solvents. For diffuse reflectance infrared Fourier transform (DRIFT), a solid sample from the nylon membrane was grinded with KBr as a support material (FTIR grade ≥ 99% from Sigma Aldrich) and then analysed with a Perkin Elmer Frontier spectrometer with the diffuse reflectance unit. For Raman spectroscopy, a Horiba LAbRAM Aramis instrument was used, with 633 nm laser line at 8 mW laser power.

Materials: Bulk MoS_2, *N*-methyl-2-pyrrolidone (NMP), and n-butyl lithium solution in hexanes (2.5 M) were purchased from Sigma Aldrich, propan-2-ol (IPA) 99.9% HPLC grade from Fisher Scientific, and $NaBH_4$ from Acros Organics. Deionised water was obtained from a PURELAB flex water purifier. All were used without further purification. Chemically exfoliated 1T-MoS_2 was synthesized following a previously reported procedure.[14]

Methods

Liquid phase exfoliation of pristine 2H-MoS_2: Pristine 2H-MoS_2 was prepared by adaptation of the method previously reported by our group.[38] As purchased MoS_2 (1.5 g) was added to IPA (75 mL, 20 g L^{-1}). The resulting mixture was sonicated with a Sonic Vibra Cell (Sonic VCX-750) with a solid tip (13 mm diameter) at amplitude 60%, pulse 6 s on/2 s off, for 1 h (time processed) with continuous ice cooling. The contents were transferred for centrifugation (Thermo Scientific Heraeus Megafuge 16 Centrifuge with a Fiberlite F15-6×100y Fixed-Angle Rotor) at 11000 rpm (13257 RCF) for 1 h. A blue supernatant containing presumed MoO_x was discarded and the sediment was redispersed in fresh IPA (75 mL). This mixture was further sonicated under the same conditions for 4 h and was subsequently centrifuged at a lower speed of 1500 rpm (247 RCF)

for 1 h to remove any unexfoliated material. The supernatant was collected as the final product, liquid exfoliated 2H-MoS_2, defined as pristine 2H-MoS_2. For electronic absorption measurements, the dispersion was diluted further with IPA in a 1:50 ratio. The absorption coefficient (69.0 $L g^{-1} cm^{-1}$) has been previously established.[38] The as-prepared dispersion had an average concentration of 0.40–0.45 mg mL^{-1}.

Preparation of negatively charged 2H-MoS_2 (n-2H-MoS_2): $NaBH_4$ (0.171 g, 4.5 mmol) was added to pristine 2H-MoS_2 in IPA (60 mL, 0.40 g L^{-1}, 1:30 2H-MoS_2:$NaBH_4$ molar ratio). This mixture was stirred under magnetic stirring at 25 °C for 24 h. The contents were centrifuged at 11000 rpm for 0.5 h and the resulting sediment was redispersed in deionised water (60 mL) through bath sonication for 0.5 h. A second centrifugation was performed at 11000 rpm for 0.5 h, allowing for the removal of presumed oxidised sulfur and molybdenum salts that were separated upon discarding of the supernatant. The sediment was redispersed in deionised water (60 mL) through bath sonication for 0.5 h which was followed by centrifugation for a final time at 700 rpm (54 RCF) for 1 h to separate any poorly dispersed particles. The supernatant was collected as the final product. The usual concentration of the final product was 0.32–0.35 g L^{-1} as determined through electronic absorption spectroscopy ($\varepsilon = 35.7(2.8)$ L $g^{-1} cm^{-1}$). For electronic absorption measurements, samples were diluted with water in a 1:50 ratio. 1:100 dilutions were used for the zeta-potential and DLS measurements. For XPS, pXRD, TGA, and DRIFT analysis, the sample was filtered through a nylon filter membrane (0.2 μm pore size) and the obtained solid was subsequently dried under vacuum for 20 min. The solid-coated membrane was left at ambient conditions (room temperature, aerobic atmosphere) for a further 24 h before any analysis. For Raman spectroscopy, the sample was drop-cast onto a silicon wafer from the original dispersion.

Determination of the electronic absorption extinction coefficient of n-2H-MoS_2: A nylon filter membrane 0.2 μm pore size was dried in the oven at 100 °C for 24 h and its mass was recorded on an analytical balance. Then the n-2H-MoS_2 dispersion (15.0 mL) was filtered through the membrane and the resulting membrane-supported solid was dried again in the oven for 24 h at 100 °C. The mass of the membrane with the sample was recorded and the concentration of the initial dispersion was determined by dividing the acquired sample mass by the filtered volume. The same original dispersion of n-2H-MoS_2 was used to prepare a series of dilutions which were examined by electronic absorption spectroscopy. The absorbance at the local minimum of $\lambda = 345$ nm for each standard was recorded and a calibration graph of absorbance vs. concentration × path length was prepared (Figure S4). The experiment was performed in triplicate to ensure accuracy. The extinction coefficient was determined as a slope of this graph and was shown to equal $\varepsilon = 35.7(2.8)$ L $g^{-1} cm^{-1}$.

Optimisation of n-2H-MoS_2 synthesis: The optimisation entailed finding the most favourable concentration of the reactants, the optimal time of the reaction, long-term stability tests, examination of potential catalysts and examining the applicability of the method to 2H-MoS_2 exfoliated in NMP.

The concentration of $NaBH_4$: Two concentrations of $NaBH_4$ in IPA dispersions of 2H-MoS_2 were examined, 75 mM and 7.5 mM which corresponds to a 1:30 and 1:3 2H-MoS_2:$NaBH_4$ molar ratio, respectively. Hence, two batches of solid $NaBH_4$ (either 0.171 g, 4.5 mmol, 75 mM or 0.0171 g, 0.45 mmol, 7.5 mM) were added to separate pristine 2H-MoS_2 dispersions (60 mL, 0.40 g L^{-1}) and were set to stir for 24 h. The samples were worked up according to the standard procedure and electronic absorption spectra of the final products were collected (Figure S5). Both samples were then stored for 1 week at 5 °C. After that time electronic absorption spectra were collected and compared against the initial spectra.

Time of reaction: Four different times of reaction were examined: 3, 5, 16 and 24 h. The standard reaction conditions and work-up were employed; solid $NaBH_4$ (0.1710 g, 4.5 mmol) was added to the pristine 2H-MoS_2 dispersion (60 mL, 0.40 g L^{-1}) and the electronic absorption spectrum of each was collected (Figure S6). From the Beer–Lambert Law, the concentrations of the acquired nanomaterial were established as 0.23, 0.26, 0.25 and 0.28 g L^{-1}, for 3, 5, 16 and 24 h mixing times, respectively. All four samples were stored at 5 °C for 100 h. After this time electronic absorption spectra were collected and compared against the initial spectra.

Long-term stability: The optimised formulation of n-2H-MoS_2 (1:30 2H-MoS_2:$NaBH_4$ molar ratio, 24 h mixing time) was set up for long term stability tests. It was stored at 5 °C for 4 days and 4 weeks. After 4 days of cold storage, the electronic absorption spectrum was collected without any pre-treatment and was compared against the initial spectrum (Figure S7). After 4 weeks of storage, some sedimentation was observed at the bottom of the vessel, thus, the sample was bath sonicated for $t = 30$ min to redisperse any partially aggregated particles and then the electronic absorption spectrum was acquired and compared against the initial spectrum (Figure S8).

$NaBH_4$ activators: Two catalysts and a change in reaction temperature were examined: methanol, acetic acid, or increasing the temperature of the reaction to 60 °C. Only upon the addition of acetic acid an immediate evolution of gas was observed. All three samples were mixed for 24 h under the otherwise standard conditions, were worked up according to the standard procedure and the electronic absorption spectra of obtained products were collected and compared against the control sample synthesised according to the standard procedure (Figure S9).

Preparation of n-2H-MoS_2 from 2H-MoS_2 exfoliated in NMP: 2H-MoS_2 was obtained by liquid-phase exfoliation in NMP according to a literature procedure.[11] $NaBH_4$ (6.5 mg, 0.17 mmol) was added to 2H-MoS_2 in NMP (45 mL, 0.02 g L^{-1}, 1:30 2H-MoS_2:$NaBH_4$ molar ratio) and this was set to stir for 24 h. The sample was worked up as normal, and the electronic absorption spectrum and the zeta-potential of the final product in H_2O were collected (Figure S10).

Preparation of electrodes: All electrodes were prepared through drop-casting 2H-MoS_2 in IPA (40 μL), n-2H-MoS_2 in H_2O (60 μL) or 1T-MoS_2 in H_2O (18 μL) onto the glassy carbon electrode. In each case 18 μg of the catalyst was deposited on the electrode (~60 μg/cm^2). Electrodes were left to dry for 1 h under ambient conditions prior to electrochemical measurements. If Nafion (10 μL, 0.5 wt%, Sigma-Aldrich) was used as a cap, the solution was drop-cast onto the catalyst-coated electrode and was left to dry for an additional 0.5 h under ambient conditions.

Electrochemical Measurements: All the electrochemical measurements were performed on a CH Instruments 600E Potentiostat. A three-electrode set-up was used with Pt wire as a counter electrode, Ag/AgCl in 3 M KCl solution as the reference electrode, and glassy carbon as the working electrode in 0.5 M H_2SO_4 electrolyte solution. Before the measurement, electrodes were cycled 40 times at 10 mV/s from 0 V to −0.8 V range. The Linear Sweep Voltammetry (LSV) was then measured from 0 V to −0.8 V at 5 mV/s. All measurements were converted against reversible hydrogen electrode (E_{RHE}), using the equation $E_{RHE} = E_{Ag/AgCl} + E^0_{Ag/AgCl} + 0.059$ pH, where $E_{Ag/AgCl}$ is the measured potential, $E^0_{Ag/AgCl} = 0.209$ V at 25 °C in 3 M KCl and the pH = 0.[59]

Acknowledgements

This publication has emanated from research conducted with the financial support of Science Foundation Ireland (SFI), Grant Numbers SFI/12/RC/2278_2 and SFI/15/RS-URF/3307 and is co-funded under the European Regional Development Fund under the AMBER award. TEM and Raman spectroscopy have been performed at the CRANN Advanced Microscopy Laboratory (AML www.tcd.ie/crann/aml/). We wish to thank Clive Downing for the collection of the TEM images. Open Access funding provided by IReL.

Conflict of Interests

The authors declare no conflict of interest.

Data Availability Statement

The data that support the findings of this study are available from the corresponding author upon reasonable request.

Keywords: dispersions · functionalisation · nanomaterials · transition metal dichalcogenide · two-dimensional

[1] Y. Jiao, A. M. Hafez, D. Cao, A. Mukhopadhyay, Y. Ma, H. Zhu, *Small* **2018**, *14*, 1800640.
[2] E. Singh, P. Singh, K. S. Kim, G. Y. Yeom, H. S. Nalwa, *ACS Appl. Mater. Interfaces* **2019**, *11*, 11061–11105.
[3] Y. Shen, Z. Dong, Y. Sun, H. Guo, F. Wu, X. Li, J. Tang, J. Liu, X. Wu, H. Tian, T.-L. Ren, *Adv. Mater.* **2022**, *34*, 2201916.
[4] S. Chen, X. Liu, J. Xiong, L. Mi, Y. Li, *Mater. Today Nano* **2022**, *18*, 100202.
[5] S. Singh, A. Modak, K. K. Pant, A. Sinhamahapatra, P. Biswas, *ACS Appl. Nano Mater.* **2021**, *4*, 8644–8667.
[6] S. Barua, H. S. Dutta, S. Gogoi, R. Devi, R. Khan, *ACS Appl. Nano Mater.* **2018**, *1*, 2–25.
[7] V. Yadav, S. Roy, P. Singh, Z. Khan, A. Jaiswal, *Small* **2019**, *15*, 1803706.
[8] A. Splendiani, L. Sun, Y. Zhang, T. Li, J. Kim, C.-Y. Chim, G. Galli, F. Wang, *Nano Lett.* **2010**, *10*, 1271–1275.
[9] M. Del Valle, M. Avalos-Borja, J. Cruz, S. Fuentes, *MRS Proc.* **1994**, *351*, 287.
[10] M. Daage, R. R. Chianelli, *J. Catal.* **1994**, *149*, 414–427.
[11] J. N. Coleman, M. Lotya, A. O'Neill, S. D. Bergin, P. J. King, U. Khan, K. Young, A. Gaucher, S. De, R. J. Smith, I. V. Shvets, S. K. Arora, G. Stanton, H.-Y. Kim, K. Lee, G. T. Kim, G. S. Duesberg, T. Hallam, J. J. Boland, J. J. Wang, J. F. Donegan, J. C. Grunlan, G. Moriarty, A. Shmeliov, R. J. Nicholls, J. M. Perkins, E. M. Grieveson, K. Theuwissen, D. W. McComb, P. D. Nellist, V. Nicolosi, *Science* **2011**, *331*, 568LP–571.
[12] V. Nicolosi, M. Chhowalla, M. G. Kanatzidis, M. S. Strano, J. N. Coleman, *Science* **2013**, *340*, 1226419.
[13] S. Manzeli, D. Ovchinnikov, D. Pasquier, O. V. Yazyev, A. Kis, *Nat. Rev. Mater.* **2017**, *2*, 17033.
[14] P. Joensen, R. F. Frindt, S. R. Morrison, *Mater. Res. Bull.* **1986**, *21*, 457–461.
[15] Z. Lai, Q. He, T. H. Tran, D. V. M. Repaka, D.-D. Zhou, Y. Sun, S. Xi, Y. Li, A. Chaturvedi, C. Tan, B. Chen, G.-H. Nam, B. Li, C. Ling, W. Zhai, Z. Shi, D. Hu, V. Sharma, Z. Hu, Y. Chen, Z. Zhang, Y. Yu, X. Renshaw Wang, R. V. Ramanujan, Y. Ma, K. Hippalgaonkar, H. Zhang, *Nat. Mater.* **2021**, *20*, 1113–1120.
[16] L. Li, X. Yu, Z. Lin, Z. Cai, Y. Cao, W. Kong, Z. Xiang, Z. Gu, X. Xing, X. Duan, Y. Song, *Adv. Mater.* **2022**, *34*, 2207392.
[17] X. Chen, X. Yang, Q. Lou, Y. Zhang, Y. Chen, Y. Lu, L. Dong, C.-X. Shan, *Nano Res.* **2022**, *15*, 4395–4402.
[18] H. Yan, L. Chu, Z. Li, C. Sun, Y. Shi, J. Ma, *Sens. Actuators Rep.* **2022**, *4*, 100103.
[19] X. He, R. Wang, H. Yin, Y. Zhang, W. Chen, S. Huang, *Appl. Surf. Sci.* **2022**, *584*, 152537.
[20] S. Bi, M. Salanne, *ACS Nano* **2022**, *16*, 18658–18666.
[21] C. Zhu, P. Liu, B. Niu, Y. Liu, W. Xin, W. Chen, X.-Y. Kong, Z. Zhang, L. Jiang, L. Wen, *J. Am. Chem. Soc.* **2021**, *143*, 1932–1940.
[22] Z. Liu, K. Nie, X. Qu, X. Li, B. Li, Y. Yuan, S. Chong, P. Liu, Y. Li, Z. Yin, W. Huang, *J. Am. Chem. Soc.* **2022**, *144*, 4863–4873.
[23] H. Wu, R. Yang, B. Song, Q. Han, J. Li, Y. Zhang, Y. Fang, R. Tenne, C. Wang, *ACS Nano* **2011**, *5*, 1276–1281.
[24] Z. Wang, A. von dem Bussche, Y. Qiu, T. M. Valentin, K. Gion, A. B. Kane, R. H. Hurt, *Environ. Sci. Technol.* **2016**, *50*, 7208–7217.
[25] J. Kaur, M. Singh, C. Dell'Aversana, R. Benedetti, P. Giardina, M. Rossi, M. Valadan, A. Vergara, A. Cutarelli, A. M. I. Montone, L. Altucci, F. Corrado, A. Nebbioso, C. Altucci, *Sci. Rep.* **2018**, *8*, 16386.
[26] V. Forsberg, R. Zhang, J. Bäckström, C. Dahlström, B. Andres, M. Norgren, M. Andersson, M. Hummelgård, H. Olin, *PLoS One* **2016**, *11*, e0154522.
[27] D. Van Thanh, C.-C. Pan, C.-W. Chu, K.-H. Wei, *RSC Adv.* **2014**, *4*, 15586–15589.
[28] M. A. Lukowski, A. S. Daniel, F. Meng, A. Forticaux, L. Li, S. Jin, *J. Am. Chem. Soc.* **2013**, *135*, 10274–10277.
[29] D. Voiry, M. Salehi, R. Silva, T. Fujita, M. Chen, T. Asefa, V. B. Shenoy, G. Eda, M. Chhowalla, *Nano Lett.* **2013**, *13*, 6222–6227.
[30] T. F. Jaramillo, K. P. Jørgensen, J. Bonde, J. H. Nielsen, S. Horch, I. Chorkendorff, *Science* **2007**, *317*, 100–102.
[31] H. Li, C. Tsai, A. L. Koh, L. Cai, A. W. Contryman, A. H. Fragapane, J. Zhao, H. S. Han, H. C. Manoharan, F. Abild-Pedersen, J. K. Nørskov, X. Zheng, *Nat. Mater.* **2016**, *15*, 48–53.
[32] A. Tuxen, J. Kibsgaard, H. Gøbel, E. Lægsgaard, H. Topsøe, J. V. Lauritsen, F. Besenbacher, *ACS Nano* **2010**, *4*, 4677–4682.
[33] C. Backes, N. C. Berner, X. Chen, P. Lafargue, P. LaPlace, M. Freeley, G. S. Duesberg, J. N. Coleman, A. R. McDonald, *Angew. Chem. Int. Ed.* **2015**, *54*, 2638–2642.
[34] K. C. Knirsch, N. C. Berner, H. C. Nerl, C. S. Cucinotta, Z. Gholamvand, N. McEvoy, Z. Wang, I. Abramovic, P. Vecera, M. Halik, S. Sanvito, G. S. Duesberg, V. Nicolosi, F. Hauke, A. Hirsch, J. N. Coleman, C. Backes, *ACS Nano* **2015**, *9*, 6018–6030.
[35] D. Voiry, A. Goswami, R. Kappera, C. de C. C. e Silva, D. Kaplan, T. Fujita, M. Chen, T. Asefa, M. Chhowalla, *Nat. Chem.* **2015**, *7*, 45–49.
[36] M. Vera-Hidalgo, E. Giovanelli, C. Navío, E. M. Pérez, *J. Am. Chem. Soc.* **2019**, *141*, 3767–3771.
[37] X. S. Chu, A. Yousaf, D. O. Li, A. A. Tang, A. Debnath, D. Ma, A. A. Green, E. J. G. Santos, Q. H. Wang, *Chem. Mater.* **2018**, *30*, 2112–2128.
[38] X. Chen, N. C. Berner, C. Backes, G. S. Duesberg, A. R. McDonald, *Angew. Chem. Int. Ed. Engl.* **2016**, *55*, 5803–5808.
[39] C. Backes, R. J. Smith, N. McEvoy, N. C. Berner, D. McCloskey, H. C. Nerl, A. O'Neill, P. J. King, T. Higgins, D. Hanlon, N. Scheuschner, J. Maultzsch, L. Houben, G. S. Duesberg, J. F. Donegan, V. Nicolosi, J. N. Coleman, *Nat. Commun.* **2014**, *5*, 4576.
[40] Y. Wang, K. Wang, C. Zhang, J. Zhu, J. Xu, T. Liu, *Small* **2019**, *15*, 1903816.
[41] U. Maitra, U. Gupta, M. De, R. Datta, A. Govindaraj, C. N. R. Rao, *Angew. Chem. Int. Ed.* **2013**, *52*, 13057–13061.
[42] G. Eda, H. Yamaguchi, D. Voiry, T. Fujita, M. Chen, M. Chhowalla, *Nano Lett.* **2011**, *11*, 5111–5116.
[43] Z. Zeng, Z. Yin, X. Huang, H. Li, Q. He, G. Lu, F. Boey, H. Zhang, *Angew. Chem. Int. Ed.* **2011**, *50*, 11093–11097.
[44] X. Chen, M. Kohring, M. Assebban, B. Tywoniuk, C. Bartlam, N. Moses Badlyan, J. Maultzsch, G. S. Duesberg, H. B. Weber, K. C. Knirsch, A. Hirsch, *Chem. A Eur. J.* **2021**, *27*, 13117–13122.
[45] X. Chen, A. M. Krajewska, C. McGuinness, A. Lynes, D. McAteer, N. Berner, G. Duesberg, J. N. Coleman, A. R. McDonald, *Chem. A Eur. J.* **2021**, *27*, 984–992.
[46] S. Mouri, Y. Miyauchi, K. Matsuda, *Nano Lett.* **2013**, *13*, 5944–5948.
[47] J. Heising, M. G. Kanatzidis, *J. Am. Chem. Soc.* **1999**, *121*, 11720–11732.
[48] R. Quirós-Ovies, M. Vázquez Sulleiro, M. Vera-Hidalgo, J. Prieto, I. J. Gómez, V. Sebastián, J. Santamaría, E. M. Pérez, *Chem. A Eur. J.* **2020**, *26*, 6629–6634.
[49] A. Jawaid, D. Nepal, K. Park, M. Jespersen, A. Qualley, P. Mirau, L. F. Drummy, R. A. Vaia, *Chem. Mater.* **2016**, *28*, 337–348.
[50] H. He, C. Gao, *Chem. Mater.* **2010**, *22*, 5054–5064.
[51] M. Doğan, A. Selek, O. Turhan, B. K. Kızılduman, Z. Bicil, *Fuel* **2021**, *303*, 121335.
[52] G. Berhault, L. Cota Araiza, A. Duarte Moller, A. Mehta, R. R. Chianelli, *Catal. Lett.* **2002**, *78*, 81–90.

[53] S. Mathew, K. Gopinadhan, T. K. Chan, X. J. Yu, D. Zhan, L. Cao, A. Rusydi, M. B. H. Breese, S. Dhar, Z. X. Shen, T. Venkatesan, J. T. L. Thong, *Appl. Phys. Lett.* **2012**, *101*, 102103.
[54] X. Chen, P. Denninger, T. Stimpel-Lindner, E. Spiecker, G. S. Duesberg, C. Backes, K. C. Knirsch, A. Hirsch, *Chem. Eur. J.* **2020**, *26*, 6535–6544.
[55] R. Canton-Vitoria, T. Scharl, A. Stergiou, A. Cadranel, R. Arenal, D. M. Guldi, N. Tagmatarchis, *Angew. Chem. Int. Ed.* **2020**, *59*, 3976–3981.
[56] S. Jiménez Sandoval, D. Yang, R. F. Frindt, J. C. Irwin, *Phys. Rev. B* **1991**, *44*, 3955–3962.
[57] D. J. Shaw, *Introduction to Colloid and Surface Chemistry*, Butterworth-Heinemann, **1992**.
[58] X. Chen, Z. Wang, Y. Wei, X. Zhang, Q. Zhang, L. Gu, L. Zhang, N. Yang, R. Yu, *Angew. Chem. Int. Ed.* **2019**, *58*, 17621–17624.
[59] L. Wang, F. Dionigi, N. T. Nguyen, R. Kirchgeorg, M. Gliech, S. Grigorescu, P. Strasser, P. Schmuki, *Chem. Mater.* **2015**, *27*, 2360–2366.

Manuscript received: June 27, 2023
Accepted manuscript online: August 3, 2023
Version of record online: September 8, 2023